Nature Communications

https://doi.org/10.1038/s41467-026-68498-x

Article in Press

Customized composition of lithium metal solid-electrolyte interphase by electric field modulation of anion motion direction

Received: 1 March 2025

Accepted: 8 January 2026

Cite this article as: Xu, S., Zheng, L., Guo, X. *et al.* Customized composition of lithium metal solid-electrolyte interphase by electric field modulation of anion motion direction. *Nat Commun* (2026). https://doi.org/10.1038/s41467-026-68498-x

Shengtao Xu, Lijun Zheng, Xiaoyu Guo, Rong Gu, Shuaiqi Gong, Jinting Xu, Sheng Zhu, Qingwei Gao, Qunjie Xu, Penghui Shi, Xin Zhao, Yulin Min & Jun Lu

Customized composition of lithium metal solid-electrolyte interphase by electric field modulation of anion motion direction

Shengtao Xu[1,+], Lijun Zheng[2,+], Xiaoyu Guo[1], Rong Gu[1], Shuaiqi Gong[1,3]*, Jinting Xu[1,2]*, Sheng Zhu[1,3]*, Qingwei Gao[1,3], Qunjie Xu[1,3], Penghui Shi[1,3], Xin Zhao[4], Yulin Min[1,3]*, Jun Lu[2]*

[1]Shanghai Key Laboratory of Materials Protection and Advanced Materials in Electric Power, Shanghai University of Electric Power, Shanghai 200090, China;

[2]College of Chemical and Biological Engineering, Zhejiang University, Hangzhou, China;

[3]Shanghai Institute of Pollution Control and Ecological Security Shanghai 200092, China

[4]College of Electrical Power Engineering, Shanghai University of Electric Power, Shanghai 200090, China

[+]These authors contributed equally

* E-mail: sq_gong@shiep.edu.cn (S.-Q. Gong), xujinting011291@shiep.edu.cn (J.-T. Xu), zhusheng@shiep.edu.cn (S. Zhu), minyulin@shiep.edu.cn (Y.-L. Min), junzoelu@zju.edu.cn (J. Lu).

Abstract: In high-voltage lithium-metal battery systems, electrolyte characteristics are crucial for achieving the optimal balance between non-flammability and battery performance. Herein, an electrolyte system based on triethyl phosphate solvent with lithium oxide difluoroborate, lithium tetrafluoroborate and lithium nitrate as solutes is proposed. TEP, as the sole solvent, ensures the inherent non-flammability of the electrolyte, while the solutes LiODFB, $LiBF_4$ and $LiNO_3$, benefit from the different binding energies of the three anions and lithium ions, to optimize the structure of the solvation shell and direction of anion movement, thereby forming a favorable interfacial phase. Consequently, solid electrolyte interphase enriched with B-O and Li_3N in the inner layer and LiF in the outer layer is formed, which improves the stability and reversibility of the lithium metal negative electrode. The Li||NCM811 cell with the as-prepared electrolyte can be stably cycled for 600 cycles at a high cut-off voltage of 4.5 V with a capacity retention of 90.19%. Even at 60°C for 600 cycles, the capacity retention rate remains at 81.18%. This work demonstrates an effective strategy for the design of high-voltage non-flammable LMBs.

Keywords: high-voltage; non-flammable; lithium metal battery; three-phase interfacial layers

Introduction

Lithium-ion batteries (LIBs) are experiencing a surge in demand for portable electronics, electric vehicles, and grid storage applications[1,2]. Currently, LIBs based on $LiCoO_2$/$LiMn_2O_4$/$LiFePO_4$ as a positive electrode and graphite as a negative electrode are approaching the upper limit of specific energy (~300 Wh kg^{-1})[3]. Employing high-energy-density positive electrode materials, such as NCM ($LiNi_xM_{1-x}O_2$, M=Mn, Co, $x > 0.8$), in conjunction with lithium metal negative electrodes is one of the most effective avenues to achieve greater specific energy (500 Wh kg^{-1})[4-7]. However, traditional carbonate-based electrolytes are not suitable for high-voltage lithium-metal batteries (LMBs) due to their poor thermal stability, flammability, and incompatibility with highly reactive lithium negative electrodes and high-voltage positive electrodes[8-10]. Therefore, the development of electrolytes that can meet the requirements of high specific energy and high safety is of vital importance and urgency.

In recent years, organophosphorus-based electrolytes (e.g. trimethyl phosphate (TMP), triethyl phosphate (TEP), and dimethyl methyl phosphonate (DMMP))[11-14] have emerged as promising candidates for LMBs due to their wide electrochemical window, temperature operating range, low viscosity, and solubility[15,16]. Nevertheless, in previous reports, batteries assembled with phosphate ester-based electrolytes have demonstrated relatively short cycle life and limited cut-off voltage. This limitation is primarily attributed to the incompatibility between organic phosphates with metallic lithium, which impedes the formation of a stable solid electrolyte interphase (SEI) on the lithium metal surface[17-19]. Mixed salt system electrolytes with rich anionic functional groups can enhance the stability of the interface layer by adjusting the composition of the interface layer, which offers a promising solution to the aforementioned issues[20-22]. From a commercial perspective, a non-flammable electrolyte comprising solely a phosphate ester as a

solvent and a suitable quantity of mixed lithium salts, offering minimal costs, stable physicochemical properties, and electrochemical stabilities, would represent an optimal electrolyte system for realizing high-voltage LMBs.

Herein, an electrolyte system is proposed to construct the optimal interfacial phase on the surface of lithium metal. The system employs TEP as the sole solvent to ensure the intrinsic non-flammable property of the electrolyte, while lithium oxide difluoroborate (LiODFB), Lithium tetrafluoroborate ($LiBF_4$), and lithium nitrate ($LiNO_3$) serve as solutes to facilitate the formation of an interfacial phase. Notably, the distinct binding energies between lithium salt anions and lithium ions (Li^+) have contributed to the optimization of the solvation shell structure. Owing to the strong binding energy of $ODFB^-$ and NO_3^- anions with Li^+, they will migrate along the direction of electric field, aggregate on the lithium metal surface, and enter the interior of the solvation shell, which will preferentially decompose to form the inner interfacial layer of B-O and Li_3N. Since the binding energy of the BF_4^- anion to Li^+ is relatively weak, it moves away from the lithium metal surface and is distributed in the outer layer of the solvation shell structure, resulting in a LiF-rich outer layer of SEI. More importantly, the formed three-phase interfacial layers serves distinct functions. LiF enhances the hardness and stability of the interfacial layer, while Li_3N boosts the ionic conductivity and facilitates ion transport[23]. The B-O species, which is a glassy component with low crystallinity, facilitates the homogeneity of the ionic flux and improves the flexibility of the SEI[24]. The Li||NCM811 full cell assembled with the electrolyte system can stably cycle 600 times at a high cut-off voltage of 4.5 V with a capacity retention of 90.19%. Even after 600 cycles at 60°C, the capacity retention remains at 81.18%. Moreover, the Li||NCM811 pouch cell achieved a high specific energy (based on the mass of the whole cell) of 430.51 Wh kg^{-1},

representing one of the highest levels among lithium metal batteries utilizing non-flammable electrolytes.

Results

Design principle of the three-phase interface layer

To comprehensively evaluate the electrochemical stability and ionic conductivity of electrolytes, linear sweep voltammetry (LSV) and the electrochemical impedance spectroscopy (EIS) were used to systematically screen electrolytes prepared by different electrolytes, salt additions and chemical-formulations. Initially, a comprehensive evaluation of electrolyte systems with a total ion concentration of 1.2 M and varying molar ratios of lithium salts was conducted. The electrolyte system with a lithium salt molar ratio of 1:1:1 exhibited the highest ionic conductivity and the widest electrochemical window, as shown in Figures S1a-b. Subsequently, further investigations were carried out on electrolyte systems with different concentrations of lithium salts at the 1:1:1 molar ratio, with a particular focus on their Li^+ conductivity. Interestingly, comparisons revealed that the 0.5 M-DBN electrolyte (a concentration of 0.5 M for each of LiODFB, $LiBF_4$, and $LiNO_3$, denoted as 0.5 M-DBN) achieved the highest ionic conductivity (Figures S1c-d). Therefore, the 0.5 M-DBN electrolyte was selected as the subject for further study.

After identifying a relatively suitable additive, further investigations into the decomposition mechanisms of the three lithium salts in the 0.5 M-DBN electrolyte were conducted using all-atom molecular dynamics (MD) simulations under a specific electric field condition. Figure 1a and b illustrate the final atomic distributions at the interface of lithium metal and electrolyte in the presence and absence of an electric field. In general, the presence of an electric field induces positively charged ions or particles to migrate in the same direction as the applied field (Figure S13), whereas negatively charged ions typically migrate in the opposite direction. Different from expectation but interesting, opposite results can be observed. As illustrated in Figure 1c and d, the distributions of $ODFB^-$ and NO_3^- anions migrate towards the negative electrode side in response

to an electric field with direction illustrated in the figure. This anomalous migration pattern is supposed to be explained by the strong binding energy between the $ODFB^-$ and NO_3^- anions and Li^+. As the anions are dragged by lithium ions moving toward the lithium surface, the probability that these two anions appear on the surface increases (Figure 1g). Consequently, at the negative electrode side, the $ODFB^-$ and NO_3^- anions are able to accept electrons from the lithium surface, resulting in the formation of a layer of Li_3N- and B-O-rich SEIs. In contrast, the BF_4^- anion moves in the direction opposite to the electric field lines due to its relatively weaker binding energy with Li^+ (Figure 1e). This lower binding energy of BF_4^- with Li^+ implies a reduced solvation energy, and the increased availability of free ions improves the overall reaction kinetics of the electrolyte. Furthermore, the TEP migrates counter to the direction of the electric field, which significantly mitigates the possibility of TEP electrolyte reduction at the negative electrode interface (Figure 1f). Meanwhile, the DFT calculations (Figure S14-15) indicate that lithium metal exhibits a preferential adsorption toward $LiNO_3$ and LiODFB. Figure 1h and Figure S16 show that the $ODFB^-$ and NO_3^- anions are strongly clustered around Li^+ with radial distribution functions (RDFs) peak positions at 1.95 Å and 1.94 Å, respectively, while the BF_4^- anion is locating at farthest distance from the lithium-ion with a peak position of 2.72 Å. The solvation structure and synergistic migration mode of the 0.5 M-DBN electrolyte lead to preferential decomposition of $LiNO_3$ and LiODFB on the lithium negative electrode surface, while meantime $LiBF_4$ undergoes partial decomposition, thus forming Li_3N- and B-O-rich inner SEIs and LiF-rich outer SEIs. The decomposition energy and order of the ternary salts was further investigated through Density Functional Theory (DFT) calculations. With high electron affinity of LiODFB (−2.58 eV) and $LiNO_3$ (−1.53 eV), a B- and N-rich SEI layer is formed on the lithium metal negative electrode, while $LiBF_4$ has trace decomposition to form a F-rich components for the SEI (Figure 1j).

Consequently, differences in binding energies between lithium ions and anions are able to locate an unequal position of these three anions in the electrolyte with field as well as distribution in the solvation shell, triggering the formation of an inner SEI layer consisting of Li_3N and B-O and an outer SEI layer consisting of LiF, which greatly overcome the solid limitation of the obstacle to form a stabilized SEI on the lithium surface by organophosphate esters (Figure 1j). Meanwhile, experimental verification using other combinations of strong and weak coordinating lithium salts further revealed the same SEI formation pattern, confirming the universality and effectiveness of this strategy (Fig. S17).

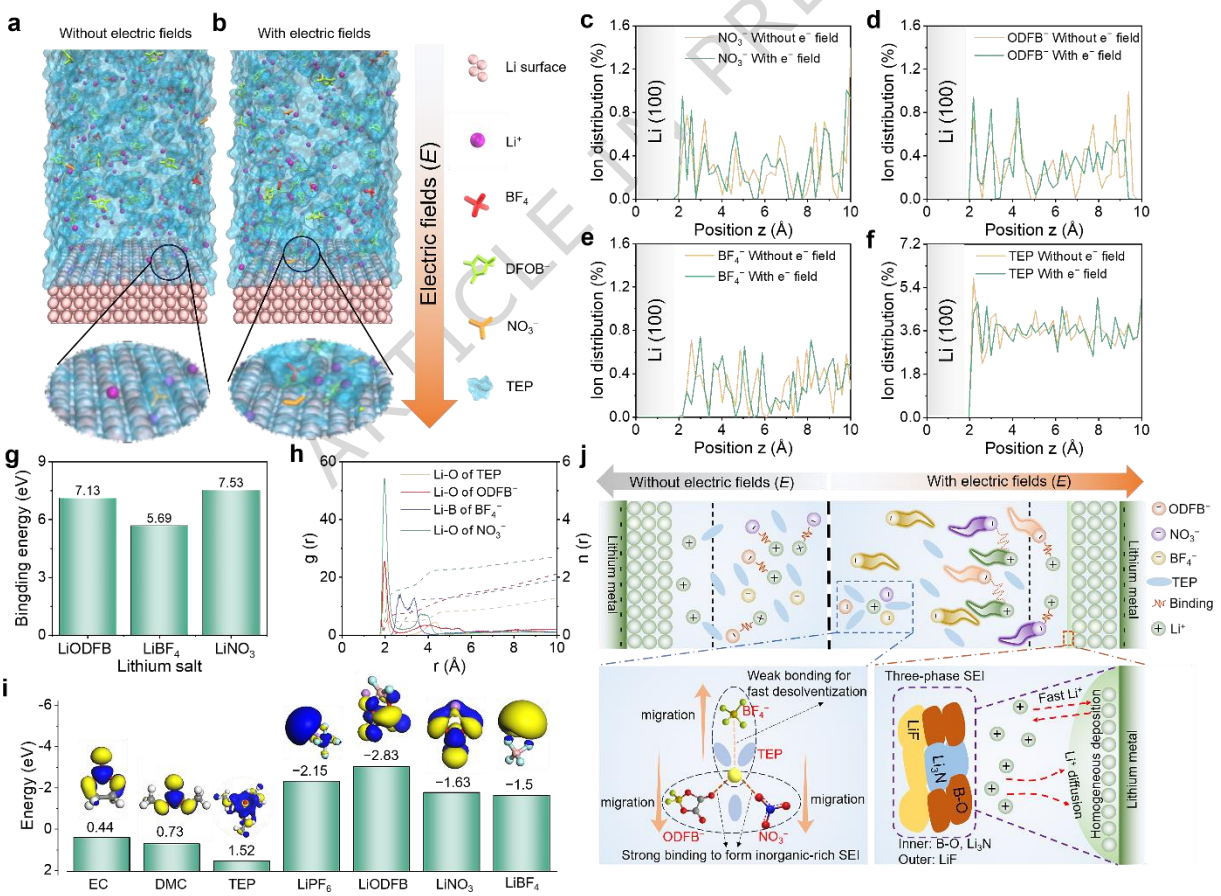

Figure 1. Electrolyte design strategy. Snapshots of the lithium-metal negative electrode electrolyte interfacial system without (a) and with (b) an electric field. The large arrow indicates the direction of the external electric field. Quantity distribution in the z-direction for each substance. (c)NO_3^-, (d)$ODFB^-$,

(e)BF_4^- and (f)TEP. (g) binding energy between Li^+ and anion part for LiODFB, $LiBF_4$ and $LiNO_3$. (h) The corresponding radial distribution function of Li^+ in 0.5 M-DBN electrolyte without an electric field was obtained by MD simulation. (i) Lowest Unoccupied Molecular Orbital **(**LUMO) energy of neutral of EC, DMC, TEP, $LiPF_6$, LiODFB, $LiNO_3$, $LIBF_4$. The yellow region represents an increase in electron density, while the blue region indicates a decrease. (j) Schematic of the electrolyte design.

Interfacial chemistry on the negative electrode side of lithium metal

The above MD simulation and DFT calculation have obtained the preliminary concept of electrolyte negative electrode interface, which provides theoretical guidance for the subsequent experimental design. Here, the SEI layer has been explored using in situ Fourier Transform Infrared spectroscopy, X-ray photoelectron spectroscopy (XPS), Atomic Force Microscopy (AFM), and Transmission Electron Microscopy (TEM). To monitor the SEI formation process, in situ infrared spectroscopy was used to study the chemical changes at the interface between the electrolyte and the lithium metal. Figure S18 shows the electrochemical performance recorded during the plating and stripping cycles of a Li||Cu cell in the in situ FTIR test. As shown in Figures 2a and S20, during the lithium deposition stage (i.e., the desolvation process), the pronounced depletion peaks at 977.90 cm^{-1} (P–O–C) and 1255.31 cm^{-1} (P=O) correspond to the gradual consumption of solvated TEP, while the emerging peak at 958.62 cm^{-1} (P–O–C) indicates the release of desolvated solvent molecules at the electrode interface[14]. Figure S19 presents the in-situ infrared spectra of the 1 M $LiPF_6$/EC–DMC electrolyte system along with the corresponding spectral analysis. Furthermore, by comparing the ratio of characteristic peak areas at the end of lithium deposition and during the stripping stage, we quantitatively analyzed the interfacial behavior of surface anions. Notably, PF_6^- (which weakly coordinates with Li^+) exhibits significantly higher reversibility than $ODFB^-$, indicating that $ODFB^-$ is more extensively

consumed in interfacial reactions (Figure 2b). These results are consistent with the theoretical calculations, indicating that the stronger binding affinity of the $ODFB^-$ anion drives it closer to the lithium surface, where it undergoes more intensive decomposition reactions and contributes to the formation of the inner interfacial layer. More interestingly, an enhanced peak at 837 cm^{-1} associated with LiF was observed, further confirming the formation of an inorganic-rich interphase (Figure S20b)[25].

To further illustrate the nanostructure of SEI, the sputtering XPS was utilized to investigate Li||NCM811 lithium negative electrode side after 100 cycles. In the F1s spectra of Figure 2c, the LiF component is dominantly found in the outer layers of the SEI. In contrast, by comparing the B1s and N1s spectra, an increased peak width and intensity of B-O and Li_3N are found with longer etching time, which indicates that they are mainly distributed in the inner part of SEI layer (Figure 2d-e). LiF could increase the stiffness of the surface and stability of the interfacial layer, while Li_3N could simultaneously enhance the ionic conductivity and facilitates ion transport (Table S2). The B-O related substances in this layer is a glassy-type matter with low crystallinity, leading homogeneity flux. In contrast, the SEI layer formed by utilizing 1 M $LiPF_6$ EC/DMC electrolyte consists mainly of LiF as an inorganic material (Figure S22a). Due to the low ionic conductivity of SEI, the transport of lithium ions is hindered, resulting in uneven deposition on the surface of the lithium negative electrode, and ultimately the formation of lithium with highly porous morphology and whisker structure. The Derjaguin-Müller-Toporov (DMT) modulus was subsequently quantified by Atomic Force Microscopy (AFM) to assess the impact of introducing B-O bonding to change the mechanical stability of SEI. Average DMT of as-formed B-O-rich SEI films by 0.5 M-DBN electrolyte was 2.12 GPa, which was 1.44 times higher than that of SEI films formed by the 1.5M-N (1.5 M of $LiNO_3$ of TEP, noted as 1.5 M-N) electrolyte (the average DMT

of 1.5 M-N was 1.47 GPa) (Figure 2f and S23). Therefore, B-O-containing SEI with high DMT modulus enables better adaptability to volume changes during the lithium plating and stripping process and thereby dismiss lithium-deformation and negative electrode fracture. Figures 2g and S24 show the atomic ratios of several elements under different etching time. It is evident that P content in the SEI layer is only 7% after 100 seconds of etching, while the B content is as high as 17% (Figure 2g). This suggests that the SEI layer in the 0.5 M–DBN electrolyte was formed mainly by decomposition of lithium salts, which correspond to a higher proportion of C and O elements in this layer, rather than the solvent TEP itself. The in-situ decomposition of $LiBF_4$ would provide a high content of F atoms in this layer, which was not found to be as high as B by estimation of XPS result. Therefore, large amount of B-O comes from the preferred and expected decomposition of LiODFB instead of other salts, consist with theory supposed by simulation. In contrast, the commercial electrolytes are usually adapting salt of $LiPF_6$ which does not contain C and O elements, and thus the layer of SEI with high C and O ratios are caused by the decomposition of EC and DMC solvents (Figure S25-S26). Overall, for the SEI formed in the 0.5M-DBN electrolyte, LiF has high interfacial rigidity to prevent the growth of lithium dendrites, and compounds such as Li_3N have high Li^+ ionic conductivity, which helps to improve the ionic transport properties of the SEI. Such multifunctional inorganic compounds together with B-O bonded highly flexible substances form a robust SEI with high ionic conductivity and high flexibility, and the resulting SEI achieves dense bulk deposition of lithium and high plating/stripping efficiency.

To further elucidate the spatial distribution of the tri-phase SEI formed in the 0.5 M-DBN electrolyte, Time-of-flight Secondary Ion Mass Spectrometry (TOF-SIMS) was employed to provide a three-dimensional visualization of the lithium negative electrode structure evolution (Figures 2h and 2i). Interestingly, LiF particles are primarily concentrated in the outer SEI, while

Li_3N and B-O species are mainly found in the inner SEI. Furthermore, the presence of this bilayer SEI structure was corroborated by cryo-electron microscopy observations (Figure S29). Overall, the nonuniform distribution of the three added anions and their specific solvation sheaths is evident, which allows for controlled decomposition sequences, as anticipated.

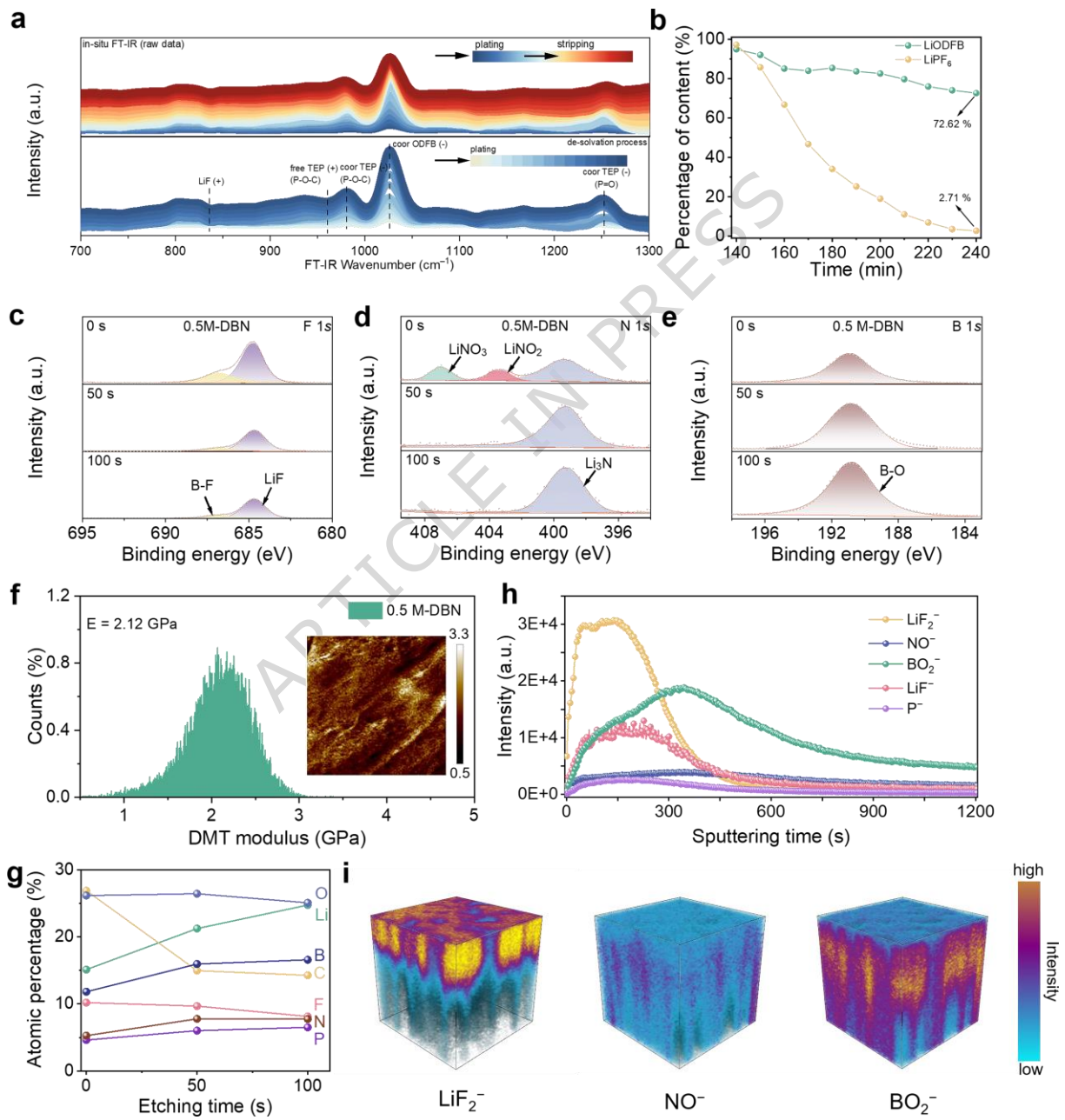

Figure 2. Interfacial chemistry of lithium metal negative electrodes cycled with different electrolytes. Contour plots of in-suit Fourier-transform infrared (FTIR) spectra at the electrode/electrolyte

interface in a 0.5 M-DBN electrolyte at 25 °C and a current density of 0.5 mA cm^{-2} (1 mAh cm^{-2}) (a) and their content variations (b). XPS depth profiles of the lithium metal anode after 50 cycles at 25 °C and 0.1 A g^{-1} using the 0.5 M-DBN electrolyte. F 1s (c), N 1s (d), and B 1s (e) spectra were recorded after 0, 50, and 100 s of sputtering. DMT modulus distribution of the SEI formed in the 0.5 M-DBN electrolyte after 50 cycles at 25 °C and a specific current of 0.1 A g^{-1} (f). Atomic concentrations of SEIs formed at different depths in the 0.5 M-DBN electrolyte (g). Time-of-flight secondary ion mass spectrometry (TOF-SIMS) depth profile of the SEI formed in the 0.5 M-DBN electrolyte after 50 cycles at 25 °C and 0.1 A g^{-1} (h), along with corresponding three-dimensional spatial maps of the SEI components (i).

Deposition of lithium metal negative electrode

To verify that the formation of a three-phase interface layer plays a key role in achieving uniform lithium deposition, the surface of the lithium negative electrode was characterized. Figure 3a shows the Coulombic efficiency (CE) of a Li||Cu half-cell assembled with the 0.5 M–DBN electrolyte to be approximately 97.22% after 100 cycles. For comparison, the CE of Li plating/stripping with the 0.75 M–DB (0.75 M LiODFB and $LiBF_4$ in TEP, denoted as 0.75 M–DB), 1.5 M–N, and 1 M $LiPF_6$/EC–DMC electrolytes are approximately 91.45%, 87.05%, and 84.52%, respectively. In addition, a Li||Cu symmetric cell assembled with the 0.5 M–DBN electrolyte demonstrated a higher CE of 99.18% after 10 Li plating/stripping cycles at a current density of 0.25 mA cm^{-2} and with an area capacity of 0.5 mAh cm^{-2}, compared to Li||Cu symmetric cells assembled with 0.75 M–DB (94.53%), 1.5 M–N (87.89%), and 1 M $LiPF_6$/EC–DMC (88.34%) electrolytes (Figure S30a), which further emphasizes the benefits of three-phase SEI formation. Furthermore, the incorporation of alternative flame-retardant additives into the 1 M $LiPF_6$ EC/DMC electrolyte resulted in markedly lower Coulombic efficiency compared to the 0.5 M-DBN-based system, thereby reinforcing the effectiveness of the proposed approach (Figure S30b). In Figure 3b and Figure S31, it can be observed that cells using the 0.75 M-DBN, 1.5 M-

N, and 1 M $LiPF_6$ EC/DMC electrolytes experienced short-circuits stopping after cycling for 680 hours, 40 hours, and 840 hours respectively, at a current density of 0.25 mA cm^{-2} and an areal capacity of 0.5 mAh cm^{-2}. In contrast to these three conditions, a battery assembled with the 0.5 M–DBN electrolyte exhibited a longer cycle life exceeding 1000 hours for Li plating/stripping, mainly due to the effective suppression of lithium dendrite growth. Similar tendencies were also observed at higher current densities, with a current density of 1 mA cm^{-2} and an areal capacity of 1 mAh cm^{-2} (Figure S32). The electrochemical performance demonstrate that the 0.5 M-DBN electrolyte is functioning in enhancing the reversibility and enlarge longer Li plating/stripping. This improvement is attributed to the formation of a robust interfacial protective layer on the lithium metal negative electrode by the tri-salt.

To directly observe lithium deposition in the electrolyte, Scanning Electron Microscopy (SEM), Scanning Probe Microscopy (SPM), and in situ electrochemical optical microscopy were used to characterize the surface of the lithium negative electrode. Figures 4c and 4d display the morphology of lithium negative electrodes after plating in 0.5 M-DBN and 1 M $LiPF_6$ EC/DMC electrolytes. The formation of lithium dendrites and the porous surface morphology is associated with low CE values and with instability in Li plating/stripping. In contrast, 0.5 M-DBN electrolyte provides dense and uniform lithium deposition, which is consistent with battery's high CE and stable Li plating/stripping performance. Similar results were also observed for Li||NCM811 cells after 100 cycles (Figure S33). Furthermore, the growth of lithium whisker-like dendrite leads to a considerable rise in porosity. This tendency is apparent in the cross-sectional SEM images, as shown by the thicknesses of the deposited lithium layers, which were 28.20 μm and 47.20 μm for cells cycled in the 0.5 M–DBN electrolyte and the commercial electrolyte, respectively (Figure 3e-f). As shown in Figure 3g–h and Figure S34, compared with the conventional 1 M $LiPF_6$

EC/DMC electrolyte system, the use of the 0.5 M-DBN electrolyte significantly reduces the thickness of the deposited layer on the lithium metal negative electrode surface, while promoting a denser and bulk-like lithium deposition morphology. Potential map analysis by scanning probes suggests that the potential distribution of the 0.5 M-DBN electrolyte is uniform. This uniform and flat in situ potential distribution prevents the formation of lithium dendrites and facilitates the uniform deposition of Li^+, where Li deposition occurs at relatively low potential. Consequently, the use of the 0.5 M–DBN electrolyte produces a dense and flattened lithium layer with minimal dendrite formation, which thus improves the CE.

Lithium deposition was monitored in battery by 0.5 M-DBN and 1 M $LiPF_6$ EC/DMC electrolytes at a current density of 1 mA cm^{-2} using in situ electrochemical microscopy (Figure 3i). The growth of dendritic crystals was observed during the deposition process using a commercial electrolyte, accumulating in the formation of a large dendritic crystal on the lithium surface after only 5 h plating. In contrast, adaption of the 0.5 M-DBN electrolyte was found to effectively inhibit the growth of dendritic crystals on the lithium surface. After deposition of 5 mAh cm^{-2}, uniform lithium deposition on the lithium surface was still observed. This uniform deposition was attributed to the formation of a highly ion-conductive SEI layer on the lithium surface, which provides high ionic conductivity at the interface and promotes uniform Li^+

deposition.

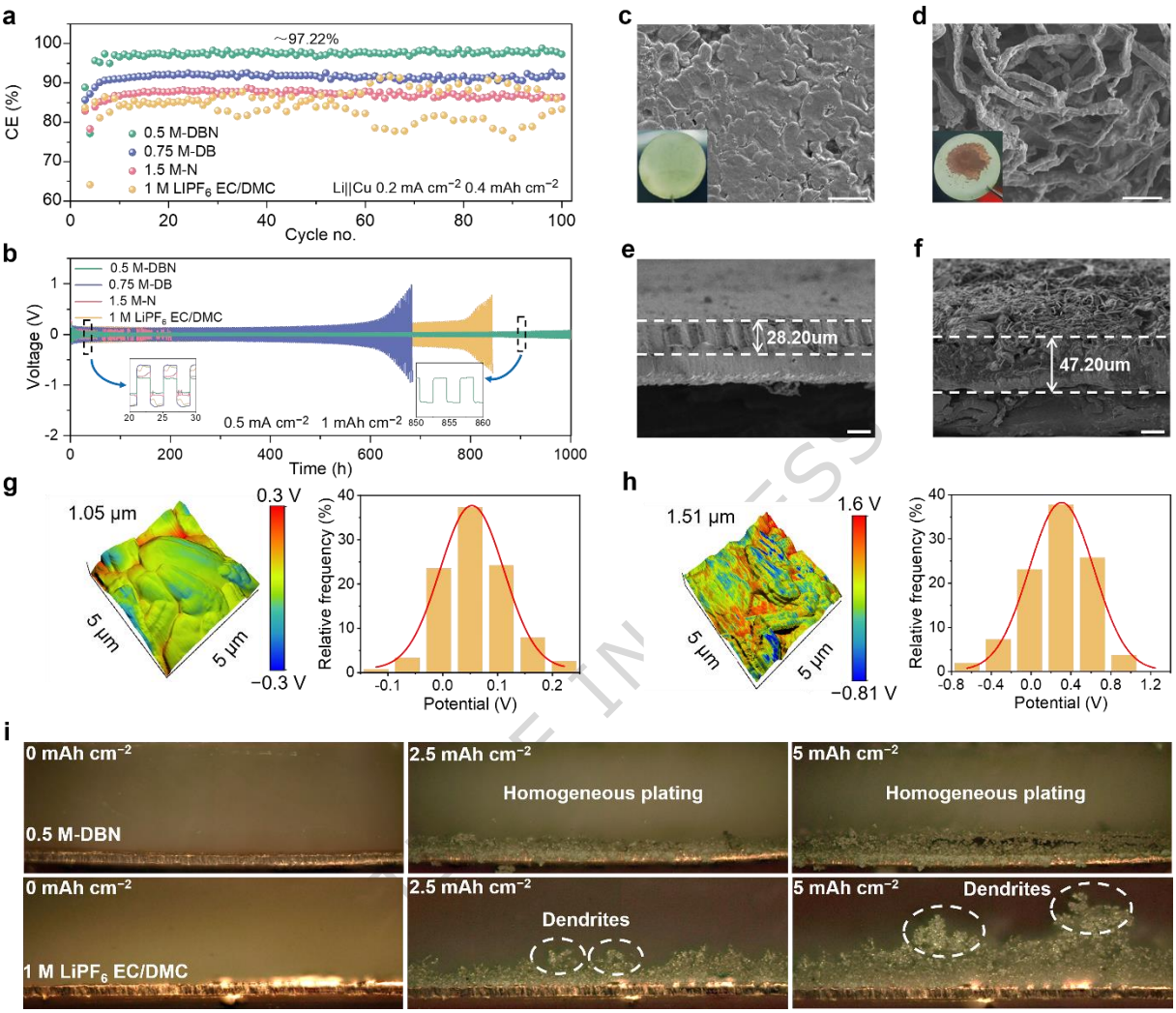

Figure 3. Optimized SEI layer for Li plating and stripping. (a) Constant-current cycling performance of Li||Li symmetric batteries with 0.5 mA cm^{-2}, 1 mAh cm^{-2}at 25°C. (b) The stability of Li||Cu cells with 0.2 mA cm^{-2}, 0.4 mAh cm^{-2} at 25 ºC. (c, d) Top-view SEM images (Scale bar: 10 μm) and (e, f) SEM cross-sectional images (Scale bar: 20 μm) of lithium deposition in 0.5 M-DBN and 1 M $LiPF_6$ EC/DMC at 0.5 mA cm^{-2} within 5 mAh cm^{-2}. (g,h) The 3D-KPFM topography and surface potential images, along with their corresponding Gaussian distribution plots, of lithium deposited on copper foil surfaces under the conditions of 25°C, 0.5 mA cm^{-2}/1 mAh cm^{-2}, using electrolytes of 0.5 M DBN and 1 M $LiPF_6$ in EC/DMC, respectively. (i) In-situ optical microscopy of lithium deposition using two electrolytes at 25 °C and current densities of 1 mA cm^{-2} (5 mAh cm^{-2}).

Interfacial chemistry on the positive electrode side of NCM811

In addition to the interface layer on the negative electrode side, nature of the cathode-electrolyte interphase (CEI) layer is equally important, which affects the stability and electrochemical properties of the battery, especially at high potentials. A stable, relatively complete and uniform CEI can ensure the stability of the structure and composition of the positive electrode interface, prevent unexpected electron transfer on the positive electrode/electrolyte interface, and hinder the side reaction between the positive electrode and electrolyte. In a rigorous float test at 4.6 V with an 8-hour retention time, the cell with the 0.5 M-DBN electrolyte had a leakage current density of 2.37 μA cm^{-2}, which was only 23% of the leakage current density observed with the 1 M $LiPF_6$ EC/DMC electrolyte (10.17 μA cm^{-2}) (Figure 4a). The float test with 0.5 M-DBN electrolyte showed a lower leakage current density, which means fewer side reactions occur on the positive electrode surface[26]. At high potentials, parasitic reactions between the delithiated positive electrode and the electrolyte accelerate the dissolution of transition metals and structural degradation, which is considered one of the major failure mechanisms of high-potential lithium-ion batteries[27,28]. Successfully decreasing the likelihood of side reactions between the 0.5 M–DBN electrolyte and the delithiated positive electrode effectively suppresses the dissolution of transition metals (Figure 4b and S35), which is expected to maintain the stability of the cell's performance.

X-ray diffraction (XRD) is a valuable and widely used technique for monitoring high-nickel positive electrode materials. XRD characterization of positive electrodes removed from cells using the 0.5 M-DBN and 1 M $LiPF_6$ EC/DMC electrolytes was conducted (Figure 4c) after 100 cycles. The XRD analysis indicates that the peak positions of the positive electrode samples are essentially unchanged after cycling with the 0.5 M–DBN electrolyte. For comparison, the positive electrodes

of batteries using commercial electrolytes show significant peak shifts, indicating a partial transformation of the interfacial layered structure into an irreversible rock salt phase. The structural evolution of the NCM811 positive electrode has been studied by in-situ XRD measurements during charge and discharge with various electrolytes. Peaks and Bragg angles of the (003) and (101) crystal planes of the NCM811 positive electrode in batteries using the commercial electrolyte demonstrate significant changes during the phase transition from the H1 phase to the M phase below approximately 3.8 V (Figure 4e and S36). It was observed that the (003) and (101) crystal planes of the NCM811 positive electrode were in the H2 phase, while the (101) crystal planes of the NCM811 positive electrode were in the H2 phase as well. After transitioning to the H2 phase, subsequently the (003) peak shifts to left (low angle) and then right (high angle), indicating a phase transition from the H2 phase to the H3 phase, and also a decrease in layer spacing[29]. In the cell using 0.5 M-DBN electrolyte, the (003) diffraction peak of the NCM811 positive electrode exhibits only a slight shift of 0.72°, compared to 0.82° for the NCM811 positive electrode in the 1 M $LiPF_6$ EC/DMC electrolyte, indicating that the CEI formed in the 0.5 M-DBN electrolyte effectively suppresses the variation in the lattice parameter c[29]. Furthermore, the smaller displacement of the (101) peak of the NCM811 positive electrode of battery using 0.5 M-DBN electrolyte during the charging process is related to the lattice parameter a (Figure 4d and S37). These findings confirm that the NCM811 positive electrode in the cell with 0.5 M-DBN electrolyte sustains a more reversible structural evolution and remains stable during cycling. Additionally, SEM images revealed significant cracks on the positive electrode of the battery using the commercial electrolyte, whereas no cracks were observed on that of the battery using the 0.5 M–DBN electrolyte (Figure S38).

To investigate why the 0.5 M–DBN electrolyte is a better match for the NCM811 positive electrode than the commercial electrolyte, we characterized the interfacial layer at the positive electrode. The CEI of the NCM811 positive electrode material was directly observed using high-resolution transmission electron microscopy (HRTEM) after cycling. The NCM811 positive electrode surface of the battery using the 0.5 M–DBN electrolyte was coated with an approximately 3.83 nm thick layer of amorphous CEI. The surrounding near-surface laminar structure remained, indicating almost no phase transition after cycling. Conversely, the NCM811 positive electrode surface of battery with commercial electrolyte exhibited a 15.8 nm thick amorphous CEI layer after cycling (Figure 4f). Figure 4g shows the XPS O1s spectra of the positive electrode surface of the battery using the commercial electrolyte, indicating that the inner and outer layers of the CEI are composed of organic matter with strong C–O and C=O signals. However, the XPS pattern of the positive electrode surface of the battery using the 0.5 M–DBN electrolyte showed opposite results and also exhibited a lattice oxygen peak in NCM811 upon initial detection, suggesting the formation of a thinner CEI (Figure 4h)[30]. We observed that in the 0.5 M-DBN electrolyte, the inner layer of the CEI exhibited a lower carbon content than the outer layer, in contrast to the commercial electrolyte, which showed the opposite trend (Fig. S39). Figure S40 displays the F1s spectra, which also confirm that the LiF content on the positive electrode surface of the battery using the 0.5 M–DBN electrolyte is higher than that of the battery using the commercial electrolyte. This verified the formation of inorganic-rich CEIs. Characteristics of CEIs show that the 0.5 M–DBN electrolyte not only has high oxidation resistance but also in situ forms a protective inorganic-rich CEI through the decomposition of the selected lithium salts, thereby lessening the direct contact between the electrolyte and the NCM811 positive electrode and effectively preventing further decomposition of the electrolyte. Thus, the rapid embedding and

detachment of lithium ions is enabled. As expected, the inorganic-rich CEI layer formed by the 0.5 M–DBN electrolyte inhibits the side reaction between the electrolyte and the nickel-rich positive electrode, resulting in improved performance at a high cutoff voltage.

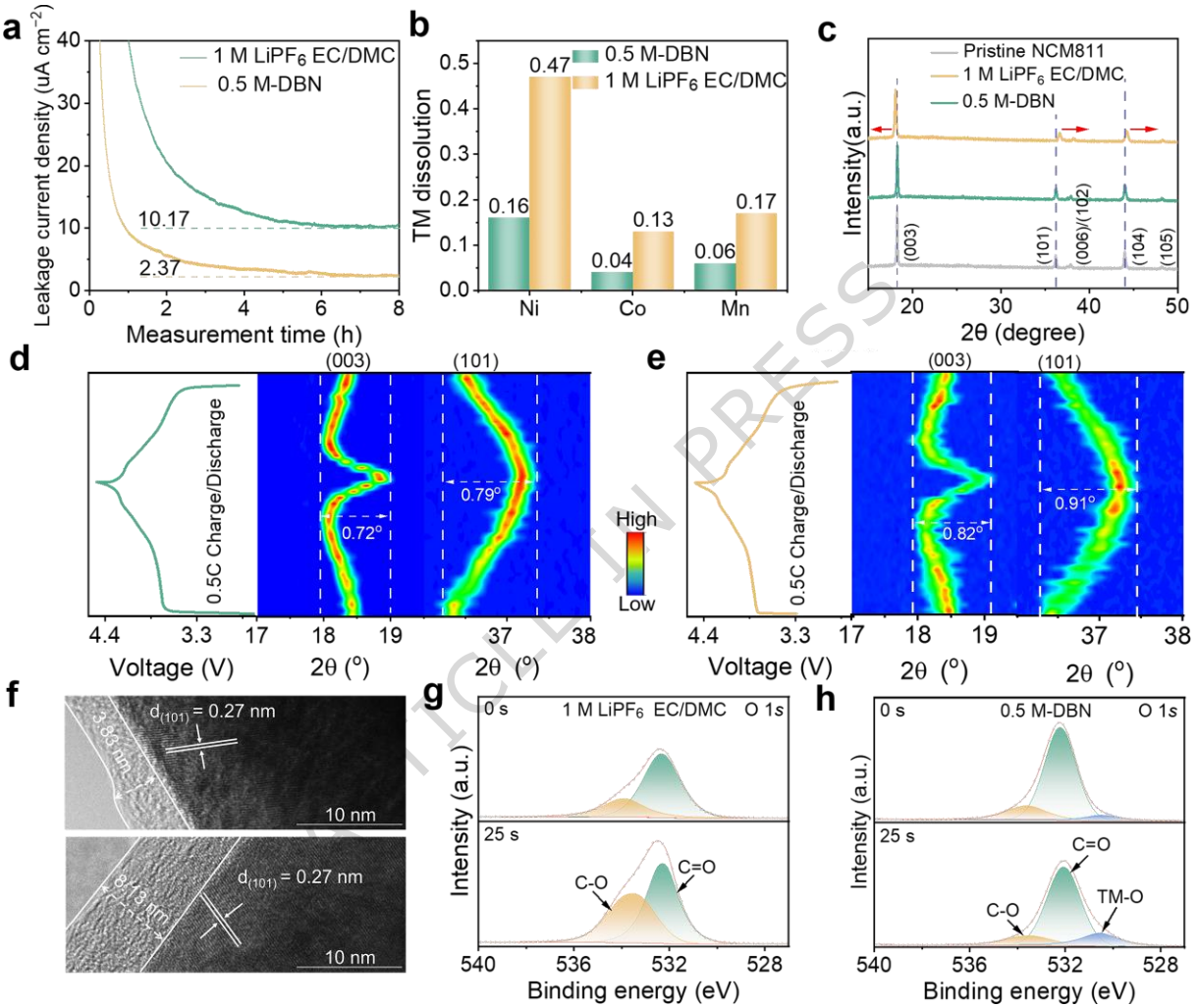

Figure 4. Oxidation stability of designed electrolyte and compatibility with NCM811 positive electrode. (a) NCM811 positive electrode leakage current density during float test after 3 cycles in the specified electrolyte under constant Potential (4.6 V vs. Li^+/Li) at 25°C. (b) Quantification of transition metal (Ni, Co, Mn) dissolution from the positive electrode material after 100 cycles at 25 °C and 0.2 A g^{-1}, measured by ICP-MS in the specified electrolyte. (c) XRD pattern of NCM811 original positive electrode and NCM811 positive electrode after 100 cycles at 25°C in the studied electrolyte. In-situ XRD pattern of the first cycle of (d) the batteries with 0.5 M-DBN and (e)1 M $LiPF_6$ EC/DMC electrolytes at 36 mA g^{-1} as

current density and 25°C. Charge-discharge curves and corresponding color-coded images of the (003) and (101) peaks are shown. (f) HRTEM images of NCM811 after 100 cycles at 25 °C and 0.2 A g^{-1} in two electrolytes (top: 0.5 M-DBN; bottom: 1 M $LiPF_6$ EC/DMC), along with the corresponding O 1s spectra (g: 1 M $LiPF_6$ EC/DMC; h: 0.5 M-DBN).

Li||NCM811 Full Cell Performance

The compatibility of the 0.5 M–DBN electrolyte with the high-voltage positive electrode was evaluated using a highly active NCM811 positive electrode. Figures 5a-c show the enhanced performance of the lithium metal full cell with the 0.5 M–DBN electrolyte compared to that with the EC/DMC-based electrolyte. In particular, the 0.5 M-DBN electrolyte demonstrated a high capacity of 205 mAh g^{-1} (based on the mass of the positive electrode), with a capacity retention rate of 87.90% after 900 cycles at a cutoff voltage of 4.3 V and a 0.2 A g^{-1}. While capacity of cell with the commercial electrolyte only retained 30.20%. At a higher cutoff voltage of 4.5 V, Figure 5d shows the improved high-voltage performance of Li||NCM811 cells with the 0.5 M–DBN electrolyte compared to 1 M $LiPF_6$ EC/DMC. Cycling of the as-made Li||NCM811 cells with 0.5 M-DBN was stable, with 90.19% capacity retention and 99.6% average CE after 600 cycles. In comparison, the commercial electrolyte showed only 48.51% capacity retention and a CE below 99% at this voltage. The large voltage drop observed at the beginning of the discharge process in Figures 5e–f could be attributed to the overpotential of the positive electrode and the increase in SEI thickness on the lithium-metal negative electrode during the cycling process. Based on a successful and suitable adaptation on the NCM811 positive electrode at both 4.3 V and 4.5 V, the designed electrolyte is also compatible with Li||NCM811 cells at a 4.6 V cutoff voltage. With the 0.5 M–DBN electrolyte, a capacity of 173.3 mAh g^{-1} (based on the mass of the positive electrode) with a retention of 78.65% was obtained after 400 cycles, and a smaller voltage decay compared to that of the commercial electrolyte was also observed (Figure S43). Obviously, in contrast, only

61.3% of the capacity was maintained in the 1 M $LiPF_6$ EC/DMC electrolyte after 400 cycles. To further understanding the performance of 0.5 M-DBN, batteries under high temperatures (60 °C) were assessed. Figure 5g-i show the stability of the Li||NCM811 full cells at 60 °C using 0.5 M-DBN and 1 M $LiPF_6$ EC/DMC electrolytes at 0.2 A g^{-1}. The capacity retention of cell with 0.5 M-DBN was 81.18% with an average CE at 99.98% after 600 cycles under 60 °C and almost no voltage drop. In contrast, the Li||NCM811 full cell with 1 M $LiPF_6$ EC/DMC electrolyte showed a rapid capacity decay during 120 cycles and unstable Coulombic efficiency.

To further elucidate the high-voltage stability of the positive electrode with the 0.5 M-DBN electrolyte and the delayed capacity decay mainly caused by phase transitions during cycling, the dQ/dV curves were evaluated at 0.1 A g^{-1}/4.5 V (Figure 5j and Figure S46). The dQ/dV curve of the battery with the positive electrode in the commercial electrolyte showed serious capacity loss and voltage decay, with its peak intensity decreasing severely during cycling. Furthermore, Galvanostatic Intermittent Titration Technique (GITT) measurements were conducted on a button cell cycled for 100 cycles (Figure 6k). Due to phase transitions, structural damage, and a more resistive interphase layer, the Li^+ diffusion coefficient on the positive electrode side was found to be much higher in the 0.5 M–DBN electrolyte than in the commercial electrolyte, suggesting a lower barrier inhibiting Li^+ from moving across the CEI formed by the 0.5 M–DBN electrolyte. Based on as-mentioned results, Figure 5m compares the performance of 0.5 M-DBN and 1 M $LiPF_6$ EC/DMC electrolyte systems in six aspects. Except for lower ionic conductivity, the 0.5 M-DBN electrolyte offers attractive features over commercial carbonate-based electrolytes, including higher safety, a wider potential window, higher cycling stability for lithium-metal batteries, higher Coulombic efficiency for Li||Cu cells, and broader operating conditions at elevated temperatures.

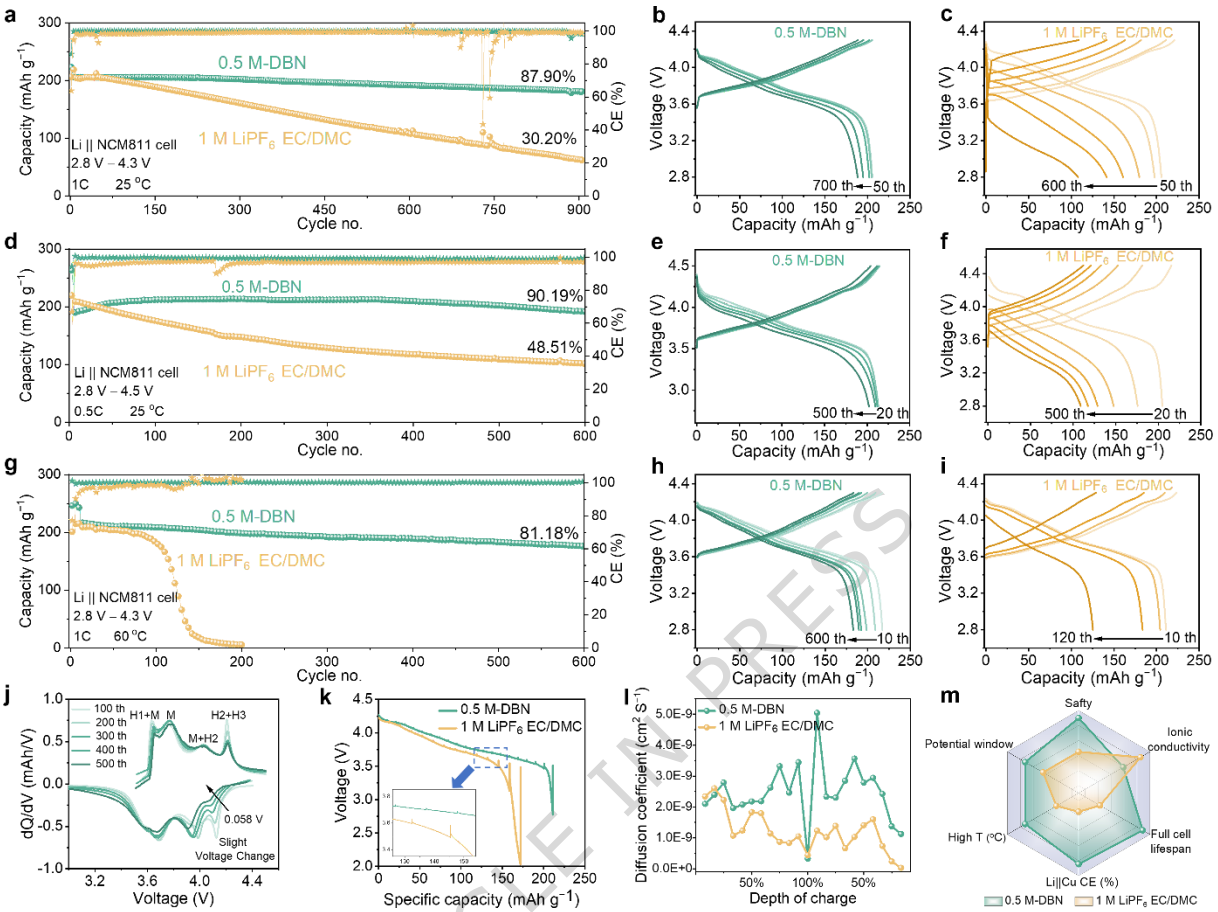

Figure 5. Electrochemical performance of LMB with NCM811 as positive electrode material at high cut-off voltage. (a) Cycling performance of Li||NCM811 cell at 0.2 A g^{-1}, 4.3 V, 25°C and (b,c) corresponding charge/discharge curve. (d) Cycling performance of Li||NCM811 cell at 0.1 A g^{-1}, 4.5 V, 25°C and (e, f) corresponding charge/discharge curve. (g) Cycling performance of Li||NCM811 cell at 0.2 A g^{-1}, 4.3 V, 60°C, (h, i) and corresponding charge/discharge curve. (j) dQ/dV curves of 0.5 M-DBN electrolyte positive electrode at 4.5 V, 0.1 A g^{-1} 25°C electrochemical conditions. (k) The GITT technique was used to measure the charge/discharge voltage profiles and (l) corresponding D_{Li+} of NCM811 positive electrode after 100 cycles with different electrolytes at 25°C. (m) Comparison of two electrolytes in terms of safety, ionic conductivity, full cell performance, Li||Cu CE (%), high-temperature performance, and potential window.

Pouch cell performance and safety assessment

Early-stage research on high-voltage Li-ion batteries concentrated on low-loading positive electrodes with excessive electrolyte and sometimes neglected the impact of realistic operational conditions during cycling[31,32]. In this study, a practical Li||NCM811 pouch cell was fabricated using a high-loading positive electrode (22 mg cm^{-2}) and a restricted amount of electrolyte (electrolyte-to-capacity ratio of 1.75 g Ah^{-1}) to implement the designed gradient SEI. The specific energy of this pouch cell was calculated by the mass of all components (Table S5). The assembled Li||NCM811 cell exhibited a specific energy (based on the mass of the whole cell) of 430.51 Wh kg^{-1}, calculated based on the mass of the full cell, and maintained a stable capacity with 84.86% retention after 83 charging/discharging cycles at 0.02 A g^{-1}, confirming the performance of the three-phase SEI design (Figure 6a-b).

In this work, utilization of 0.5 M-DBN is expected to improve the flame-retardant properties of the electrolyte. The heat resistance of the post-cycled lithium negative electrode and NCM811 positive electrode was measured by Differential Scanning Calorimetry (DSC). As shown in Figure 6c, a heat absorption peak at 187°C could be observed on both the Cycled Li/0.5 M-DBN and Cycled Li/1 M $LiPF_6$ EC/DMC, mainly caused by lithium. Moreover, the commercial electrolyte showed a large exothermic peak with a heat release of 1470.23 J g^{-1} immediately following the lithium absorption peak, which could be attributed to the reaction between highly active lithium flakes and the electrolyte. In contrast, the exothermic peak of the Cycled Li/0.5 M-DBN mixture was obviously delayed to 263°C and the exothermic was reduced to 178.03 J g^{-1}. On the positive electrode side, Figure 6d shows that the exothermic heat of the commercial electrolyte in contact with the fully charged NCM811 positive electrode is 1161.66 J g^{-1}, while the exothermic heat of the 0.5 M-DBN electrolyte is only 421.58 J g^{-1}, showing the same trend of higher stability of 0.5

M-DBN at the negative electrode. The measured exothermic data showed that dangerous reactions at both the positive and negative electrodes were effectively suppressed by 0.5 M-DBN.

The hazards of pouch cells usually arise from possible and dangerous reactions between deep-delithiated positive electrodes and the electrolyte, especially between highly oxidizing Ni sites in the positive electrode and organic compounds in the electrolyte, which inhibits the practical application of NCM811 positive electrodes[32,33]. To further demonstrate the successful formation of a safe CEI on the positive electrode side, we examined the structural changes in the fully charged positive electrode from cells with 0.5 M-DBN and 1 M $LiPF_6$ EC/DMC electrolytes by in-situ elevated XRD[34,35]. Notably, as shown in Figure 6e-f, the 0.5 M-DBN electrolyte increased the critical transition temperature from 170 °C to 200 °C, effectively delaying the onset of structural collapse and oxygen release from the NCM811 positive electrode under high-temperature conditions, which corresponds to higher overall battery safety. Enhanced thermal stability on the positive electrode side results from a robust CEI facilitated by the 0.5 M-DBN. Combustion tests were conducted on 0.5 M-DBN and 1 M $LiPF_6$ EC/DMC electrolytes, as depicted in Figure 6g, illustrating an obvious difference. Commercial electrolytes are highly flammable, and can be easily ignited with a lighter. In contrast, the 0.5 M-DBN electrolyte produces only a small amount of smoke when exposed to a flame, demonstrating its safety attributes.

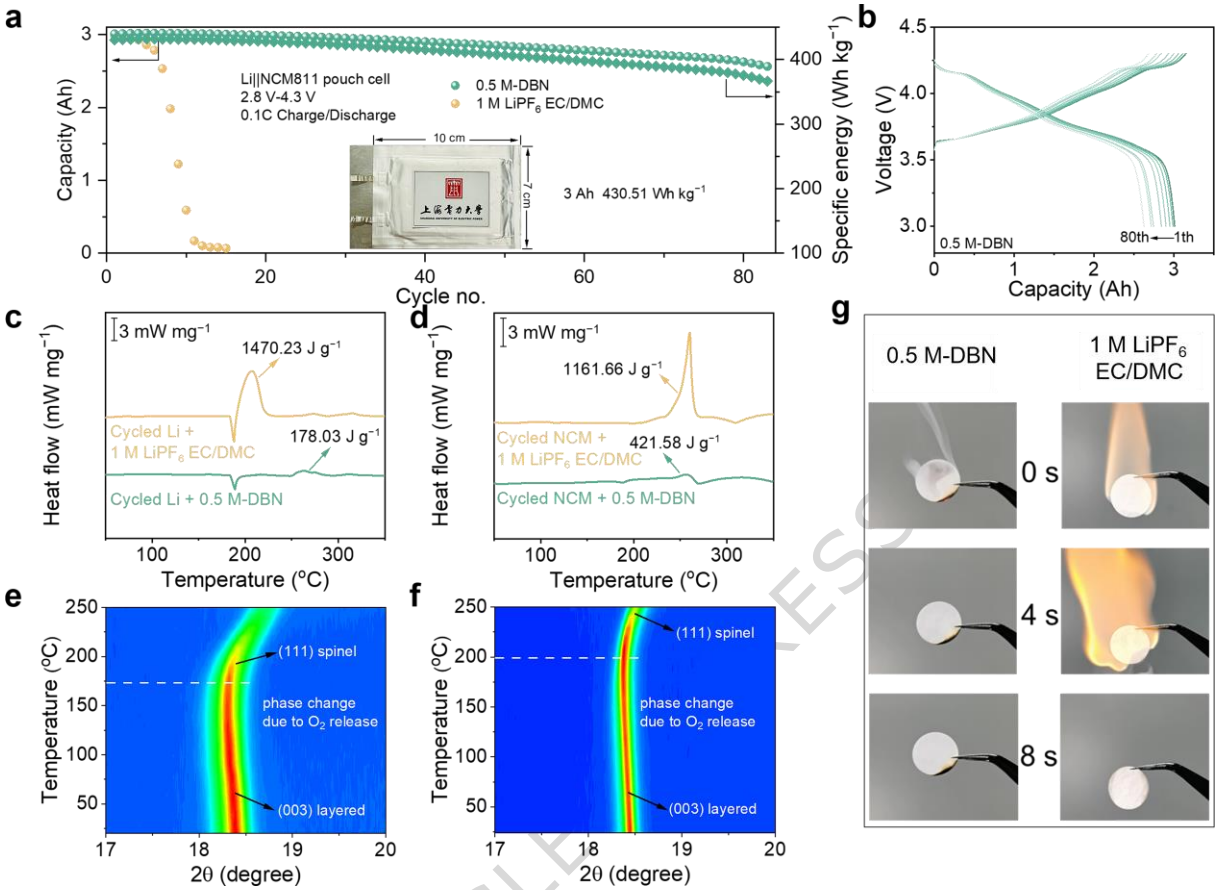

Figure 6. Pouch Cell Performance and Safety with 0.5 M-DBN Electrolyte. (a) Cycling performance and (b) capacity-voltage curves of the Li||NCM811 pouch cell at 0.02 A g^{-1} charge/discharge, 25°C. The inset shows the optical image of the corresponding pouch cell. DSC curves of (c) cycled Li and (d) cycled NCM within different electrolytes. In-situ XRD results of fully charged (e) 1 M LiPF6 EC/DMC and (f) 0.5 M-DBN electrodes during heating process. (g) Flammability testing of electrolyte.

In summary, TEP is utilized as the solvent to ensure the intrinsic non-flammability of the electrolyte, while LiODFB, $LiBF_4$, and $LiNO_3$ serve as solutes to enhance the formation of an optimal interfacial phase. The different binding energies between the added anions and the lithium ions refines the position of the triple salt aggregation in the battery system and the solvation sheath. By calculation and simulation, the $ODFB^-$ and NO_3^- anions, due to their strong binding energies to the lithium ions, are more uniformly distributed on the lithium surface and also get access to the

inner part of the solvation sheath layer, where they are preferentially decomposed. Due to the relatively weak binding energy of the BF_4^- anion to the lithium-ion, it is predominantly distributed in the outer layer of the dissolution sheath, where it decomposes to a small extent to form LiF. In addition, the weak binding energy results in a relatively low dissolution energy, which accelerates the reaction kinetics of the electrolyte. Combined with the NCM811 positive electrode, the Li||NCM811 full cell can withstand 600 cycles at a high cutoff voltage of 4.5 V with 90.19% capacity retention. Even after 600 cycles at 60°C, capacity retention is 81.18%. Moreover, the pouch cell utilizing the 0.5M-DBN non-flammable electrolyte attained a high specific energy of 430.51 Wh kg^{-1}, based on the mass of the whole cell, along with a prolonged cycle life of 83 cycles. This ternary salt engineering strategy offers a approach to the design of high-voltage, non-flammable LMB.

Methods

Materials

The following materials were procured from Shanghai Aladdin Bio-Chem Technology Co., Ltd.: Lithium difluoro(oxalato)borate (LiDFOB, ≥ 99%), Lithium Tetrafluoroborate ($LiBF_4$, 98%), Lithium nitrate ($LiNO_3$, 99%), Lithium Hexafluorophosphate ($LiPF_6$, 97%) Triethyl phosphate (TEP, 99.5%), Ethylene carbonate (EC, > 99.5%), Dimethyl carbonate (DMC, > 99%), and N-methyl-2-pyrrolidone (NMP, > 99.5%). The active material, $LiNi_{0.8}Co_{0.1}Mn_{0.1}O_2$ (NCM811) powder, polyvinylidene fluoride (PVDF, molecular weight ~1,100,000, purity ≥ 99.5%), Super P Li (particle size: 40-50 nm, purity ≥ 99.5%; powder conductivity: 10-15 S cm^{-1}), and carbon-coated aluminum current collectors (thickness: 15 μm) were all supplied by Keruode Co., Ltd. The polypropylene (PP) separator used in this study was obtained from the Guangdong Canrd New Energy Technology Co., Ltd. It has a thickness of 16 ± 2 μm, lateral dimensions of 88 mm × 10

m, a porosity of 38–40%, and a puncture strength of ≥ 280 gf. Lithium metal (battery grade, ⩾ 99.9% purity, metals basis, 15.6 mm in diameter, 100 μm) was purchased from Innochem. The materials received were immediately used to prepare the corresponding electrolytes and handled in an Ar-filled glove box (water and oxygen content < 1.0 ppm).

Electrolyte and negative electrode material preparation

(1) 0.5 M-DBN electrolyte: 0.5 M LiDFOB,0.5 M $LiBF_4$,0.5 M $LiNO_3$ salt was dissolved in blended TEP. Then put it on a stirring table and stir it until it is clear and transparent to obtain 0.5 M-DBN electrolyte. (2) 0.75 M-DB electrolyte: 0.75 M LiDFOB,0.75 M $LiBF_4$ salt was dissolved in blended TEP. Then put it on a stirring table and stir it until it is clear and transparent to obtain 0.75 M-DB electrolyte. (3) 1.5 M-N electrolyte: 1.5 M $LiNO_3$ salt was dissolved in blended TEP. Then put it on a stirring table and stir it until it is clear and transparent to obtain 1.5 M-N electrolyte. (4) 1 M $LiPF_6$ EC/DMC electrolyte: 1 M $LiPF_6$ salt was dissolved in blended ethylene carbonate (EC) and dimethyl carbonate (DMC) solvents with a volume ratio of 1:1. The NCM811 electrode was obtained by coating the slurry of NCM811 powders, acetylene black and poly(vinylidene difluoride) with a weight ratio of 8:1:1 in N-methyl-2-pyrrolidone solvent onto an aluminum current collector. Dry the slurry for 8 h at 80 °C and punch into disks with a diameter of 14 mm. The average mass loading of NCM811 is 3~5 mg cm^{-2}.

Cell assembling

All coin cells were assembled in the Argon-filled glove box with a water and oxygen content of less than 0.1 ppm. Li||Li CR-2032 type coin cells were assembled in the following order: positive electrode shell, Li-metal sheet, Celgard PP separator (16 mm), Li-metal sheet, gaskets, splinter, and negative electrode shell. Li||Cu CR-2032 type coin half-cells were assembled in the following order: positive electrode shell, Cu foil (14mm), Celgard PP separator (16 mm), Li-metal

sheet, gaskets, splinter, and negative electrode shell. Both Li||Li symmetrical cells and Li||Cu half-cells were added with 60 μL electrolyte. Li||NCM full cell assembly followed the order: positive electrode case, NCM positive electrode disk, Celgard PP separator (16 mm), Li-metal sheet, gaskets, splinter, and negative electrode shell (a total of 60 μL electrolyte was added to the cell).

The Li||NCM811 pouch cell (10.0 × 7.0 cm^2) was assembled in a dry room with a dew point 25 °C. The cell was constructed by stacking eight double-side coated positive electrode layers (NCM811, areal loading: 22 mg cm^{-2} per side) and nine metallic lithium negative electrode layers (50 μm thickness on Cu collector) in a staggered sequence, separated by a polyethylene separator. This configuration corresponded to a total theoretical capacity of approximately 3.0 Ah. The tabs for current collection were made of aluminum for the cathode and copper for the anode. An electrolyte was injected into the dry cell by weight prior to the final heat sealing, with a controlled electrolyte-to-capacity (E/C) ratio of 1.75 g Ah^{-1} (total electrolyte weight: 5.25 g). The cell was then subjected to a vacuum soaking period to ensure complete wetting of the electrodes and separator. Any residual gas generated during the subsequent formation process was evacuated under vacuum before the pouch was hermetically final-sealed to ensure cell compactness. The final cell delivered a discharge capacity of 3.0 Ah with an average voltage of 3.8 V, resulting in an Specific Energy of 430.5 Wh kg^{-1} (total cell mass: 26.48 g). For the cycling performance evaluation, all cells were tested under a fixture applying an external stack pressure of 0.5 MPa to maintain optimal interfacial contact and electrode stability.

Depth Profiling XPS

XPS test samples were prepared using Li||NCM811 Li-Metal full cells with different electrolytes (0.5M-DBN and 1M $LiPF_6$ EC/DMC) (cycling at a multiplicity of 0.1C and 10 cycles). The post-cycling lithium negative electrode and NCM811 positive electrode were then subjected

to XPS testing. XPS data were collected using Thermo Scientific K-Alpha+. The vacuum in the analysis chamber was approximately 2×10^{-7} mbar, X-ray source: monochromatic Al Kα source, energy: 1486.6 eV, voltage: 12 kV, beam current: 6 mA, analyzer scanning mode: CAE, work function: 0.5 mA cm^{-2} and 0.25 mA cm^{-2}: CAE, work function: 4.2 eV. All peaks were calibrated with the C-C bond peak as a reference. The peak was set to 284.8 eV. In addition, high-resolution scans were performed for the following regions: B1s, C1s, F1s, N1s, O1s, and P 2p. Depth profiling XPS was performed at an etch rate of 0.2 nm/s.

In-situ Fourier transform infrared spectroscopy

We executed in situ FTIR spectroscopy experiments on an IR Tracer-100. To establish a good electrical contact and to ensure an intimate interface between the cathode surface and the germanium crystal, we placed a copper mesh as a working electrode on the surface of the germanium crystal and used a lithium metal foil as a counter electrode and a reference electrode, which were attached to a stainless steel (SS316) spacer. We used an electrolyte containing 0.5 M-DBN and 1 M $LiPF_6$ EC/DMC. To enhance the intensity of the FTIR signal, we used SS316 rods to press the lid onto the coin cell when it was closed, ensuring good electrical contact between the electrodes. After completing the assembly, we let the cell sit for 6 hours. We then performed in situ electrostatic discharge and charging experiments using an IVIUM electrochemical workstation. At a current density of 0.5 mA cm^{-2}, we performed 2 h of in-situ cell discharge and 2 h of charging and collected FTIR data in real-time to record changes during cycling.

In-situ X-ray diffraction

structural changes during electrolyte charging and discharging. Specifically, a thin aluminum window (12 μm thick) was fixed as a transparent window on the cathode side of the cell. The cathode was mounted at the bottom of the cell with the active material facing up. A

uniform drop of 40 μL of electrolyte was placed on a glass fiber filter separator (GF/A, Whatman). We then performed in situ electrostatic discharge and charging experiments using the IVIUM electrochemical workstation. We performed charging and discharging at a multiplicity of 0.5C and collected XRD data in real-time to document changes during cycling.

In-situ microscopic imaging lithium-ion battery (LIB-MS-R)

Ltd. provides the LIB-MS-R device, which is specialized equipment designed to simulate and observe the growth and corresponding changes of lithium dendrites in lithium-ion button batteries. By precisely controlling the experimental conditions and parameters, the device provides a reliable experimental platform for studying the formation of dendrites in lithium-ion batteries, the growth mechanism, and the correlation with battery performance.

Transmission electron microscope and scanning electron microscope sample preparation process

For post-mortem analysis, all cyclic cathodes and anodes are removed directly from the cell. They were washed in ethylene glycol dimethyl ether and required drying for at least 12 hours after the washing was completed. The NCM cathodes used for postmortem analysis were obtained after 100 cycles at 1C multiplicity with different electrolyte conditions at a temperature of 25°C. SEM samples were obtained by lithium deposition at 25°C (deposition temperature of 25°C, deposition current density, and capacity of 0.5 mA/cm^2, respectively). The morphology and particle size of the samples were examined by FESEM.TEM and HR-TEM samples were obtained by lithium deposition at 25°C (deposition temperature of 25 °C, deposition current density, and capacity of 0.01mA/cm^2 and 0.1mAh/cm^2, respectively). A commercially available perforated carbon TEM mesh was used as the working electrode for lithium metal plating in the button cell device. After lithium metal deposition and disassembly of the button cell, the excess electrolyte was removed

from the TEM grids by using a double-sided suction cloth in an argon-filled glove box, followed by liquid nitrogen vitrification to prevent exposure to air.

Electrochemical testing

The electrochemical data for this study were collected using CR-2032 coin cell. These batteries were assembled in an Ar-filled glove box with oxygen and water concentrations maintained below 0.01 ppm. Ambient data points were obtained by storing the batteries in a Neware thermostat box during testing at 25 °C and 60 °C, respectively. Before testing, the cells were equilibrated at 25 °C for at least 10 hours. The 25 °C potential tests were conducted using a Neware BTS 4000 system, while the electrostatic potential tests were performed using a CHI-760E instrument. Electrochemical impedance spectroscopy (EIS) measurements were performed over a frequency range from 1 MHz to 100 mHz using a 5 mV AC excitation signal. The data acquisition density was set to 12 points per frequency decade. Prior to the EIS measurements, the cells were held at open-circuit voltage (OCV) for 1000 s to ensure voltage stabilization. Cyclic voltammetry (CV) was performed at a scan rate of 0.1 mV s^{-1} using a Chenhua electrochemical workstation. For the linear sweep voltammetry (LSV) test, carbon-coated aluminum foil (c-Al foil) served as the working electrode, and a scan rate of 1 mV s^{-1} was used. The cell was cycled from 2 V to 6 V (for Li/Li^+), followed by stable cathodic scans as LSV curves for each lithium-aluminum-foil cell under different electrolytes.

A custom two-electrode coin cell configuration was employed to determine the ionic conductivity of the electrolyte. In this setup, two stainless steel electrodes were symmetrically arranged with 0.027-inch-thick PTFE spacers placed between them. A fiberglass separator fully saturated with the electrolyte was confined within the cell gasket to maintain a well-defined and constant electrode contact area. The ionic resistance (R) of the electrolyte was obtained via

electrochemical impedance spectroscopy (EIS). The conductivity (σ) was then calculated using the expression σ =L/(A*R), where L denotes the distance between the electrodes and A represents the known contact area of the electrode surface. All measurements were performed inside a JHY-H-50L thermal chamber across a temperature range from 0 °C to 80 °C. Prior to each impedance measurement, the cell was held at the target temperature for one hour to ensure thermal equilibrium.

The cationic transference number (t_+) for each electrolyte was evaluated via potentiostatic polarization, a widely adopted electrochemical technique. Measurements were conducted on a CHI-760E workstation using a symmetric Li||Li cell assembled with five layers of Celgard separator. A fixed voltage of 10 mV was applied over 10,000 s to monitor current evolution. Two distinct current readings were recorded: the initial current (I_0), corresponding to the total ionic flux under uniform cation distribution, and the steady-state current (I_{ss}), which reflects contributions solely from Li^+ migration after polarization. Electrochemical impedance spectroscopy (EIS) was performed immediately before and after the polarization step to extract the corresponding cell resistances (R_0 and R_{ss}). The cation transference number was then determined according to the expression $t_+ = \frac{I_{SS}(\Delta V - I_0 R_0)}{I_0(\Delta V - I_{SS} R_{SS})}$, where ΔV denotes the applied polarization potential (10 mV).

Calculation details

The molecular dynamics (MD) simulations were carried out using the GROMACS 2024 package. Atomic interactions within the systems were modeled with the OPLS-AA force field, while cross-interaction LJ parameters were determined via the Lorentz-Berthelot mixing rules. Electrolyte molar ratios, taken from the experimental section of this study, are provided for the four MD models in Table S1. Periodic boundary conditions were applied in all three directions. Long-range electrostatic interactions were computed using the Particle Mesh Ewald (PME)

method with a real-space cutoff of 1.2 nm, which was also used as the cutoff distance for short-range van der Waals interactions.

The simulation systems were initialized using Packmol. After energy minimization, all models underwent a two-step equilibration protocol: a 2 ns NPT ensemble simulation followed by a 15 ns NVT ensemble simulation. Subsequent production runs were performed for 5 ns under NVT conditions with a 2 fs time step, and coordinates were recorded every 0.2 ps. Temperature was held constant at 298.15 K using the Nosé-Hoover thermostat, while pressure was maintained at 1 bar through the Berendsen coupling method during NPT equilibration. To enable comparative analysis, an external electric field of −1.0 V/nm was applied along the z-axis during NVT simulations. Although this field strength is higher than typical experimental values, such magnitudes are widely adopted in computational studies to generate observable responses within practical simulation timescales. Structural visualization was conducted with VMD, and detailed simulation datasets are provided in Supplementary Data 1.

Adsorption energies were investigated through density functional theory (DFT) calculations performed with the Vienna Ab initio Simulation Package (VASP). The Perdew–Burke–Ernzerhof generalized gradient approximation (PBE-GGA) was adopted for the exchange–correlation functional. Electron–ion interactions were treated using the projector augmented-wave (PAW) method, and a plane-wave cutoff energy of 450 eV was applied throughout. To mimic the influence of voltage, uniform external electric fields of 0, −0.1, and −1 V/nm were introduced along the vacuum direction. Structural optimizations were carried out until the Hellmann–Feynman forces fell below 0.02 eV $Å^{-1}$ and the energy variation between successive steps was less than 10^{-5} eV. Dispersion corrections were included via Grimme's DFT-D3 scheme to properly describe van der Waals interactions in the adsorption models. Transition states were located using the nudged

elastic band (NEB) method available in VASP. The adsorption energy for each system was evaluated according to the relation E (binding) = E(A) + E(B) - E(AB), where E(A) and E(B) represent the single-point energies of the isolated substrates, and E(AB) denotes the total energy of the adsorbed system. The detailed outcomes of the DFT calculations can be found in Supplementary Data 2.

Data availability

All data that support the findings of this study are presented in the manuscript and Supplementary Information, or are available from the corresponding author upon request. Source data are provided with this paper.

References

1 Goodenough, J. B. & Kim, Y. Challenges for rechargeable Li batteries. *Chem. Mater.* **22**, 587-603 (2010).

2 Xu, J. *et al.* Electrolyte design for Li-ion batteries under extreme operating conditions. *Nature* **614**, 694-700 (2023).

3 Li, H. Practical evaluation of Li-ion batteries. *Joule* **3**, 911-914 (2019).

4 Lin, Z., Liu, T., Ai, X. & Liang, C. Aligning academia and industry for unified battery performance metrics. *Nat. Commun.* **9**, 5262 (2018).

5 Lin, D., Liu, Y. & Cui, Y. Reviving the lithium metal anode for high-energy batteries. *Nat. Nanotechnol.* **12**, 194-206 (2017).

6 Mao, M. *et al.* Anion-enrichment interface enables high-voltage anode-free lithium metal batteries. *Nat. Commun.* **14**, 1082 (2023).

7 Liu, J. *et al.* Pathways for practical high-energy long-cycling lithium metal batteries. *Nat. Energy* **4**, 180-186 (2019).

8 Wang, Z. *et al.* Advanced ultralow-concentration electrolyte for wide-temperature and high-voltage Li-metal batteries. *Adv. Funct. Mater.* **32**, 2112598 (2022).

9 Lv, L. *et al. A low-concentration sulfone electrolyte enables high-voltage chemistry of lithium-ion batteries*. (OAE Publishing Inc., 2022).

10 Zhang, X. *et al.* A dicarbonate solvent electrolyte for high performance 5 V-Class Lithium-based batteries. *Nat. Commun.* **15**, 536 (2024).

11 Niu, C. *et al.* High-energy lithium metal pouch cells with limited anode swelling and long stable cycles. *Nat. Energy* **4**, 551-559 (2019).

12 Zeng, Z. *et al.* Non-flammable electrolytes with high salt-to-solvent ratios for Li-ion and Li-metal batteries. *Nat. Energy* **3**, 674-681 (2018).

13 Zheng, Q. *et al.* A cyclic phosphate-based battery electrolyte for high voltage and safe operation. *Nat. Energy* **5**, 291-298 (2020).

14 Guo, Q. *et al.* Bidirectional Interphase Modulation of Phosphate Electrolyte Enables Intrinsic Safety and Superior Stability for High-Voltage Lithium–Metal Batteries. *ACS nano* **17**, 24227-24241 (2023).

15 Liao, C. *et al.* Non-flammable electrolyte with lithium nitrate as the only lithium salt for boosting ultra-stable cycling and fire-safety lithium metal batteries. *Adv. Funct. Mater.* **33**, 2212605 (2023).

16 Zhu, M. *et al.* An in-situ formed stable interface layer for high-performance sodium metal anode in a non-flammable electrolyte. *Energy Storage Mater.* **42**, 145-153 (2021).

17 Zeng, Z. *et al.* Safer lithium ion batteries based on nonflammable electrolyte. *J. Power Sources* **279**, 6-12 (2015).

18 Feng, J., Ma, P., Yang, H. & Lu, L. Understanding the interactions of phosphonate-based

flame-retarding additives with graphitic anode for lithium ion batteries. *Electrochim. Acta* **114**, 688-692 (2013).

19 Nakagawa, H. *et al.* Electrochemical Raman study of edge plane graphite negative-electrodes in electrolytes containing trialkyl phosphoric ester. *J. Power Sources* **212**, 148-153 (2012).

20 Li, S. *et al.* Structured solid electrolyte interphase enable reversible Li electrodeposition in flame-retardant phosphate-based electrolyte. *Energy Storage Mater.* **42**, 628-635 (2021).

21 Liu, J. *et al.* Exceptional Li-Rich Mn-Based Cathodes Enabled by Robust Interphase and Modulated Solvation Microstructures Via Anion Synergistic Strategy. *Adv. Energy Mater.* **13**, 2300680 (2023).

22 Su, H. *et al.* Achieving Practical High-Energy-Density Lithium-Metal Batteries by a Dual-Anion Regulated Electrolyte. *Adv. Mater.* **35**, 2301171 (2023).

23 Kim, S. *et al.* Stable electrode–electrolyte interfaces constructed by fluorine-and nitrogen-donating ionic additives for high-performance lithium metal batteries. *Energy Storage Mater.* **45**, 1-13 (2022).

24 Zhu, Q. *et al.* A 110 Wh kg− 1 Ah-level anode-free sodium battery at −40°C. *Joule* **8**, 482-495 (2024).

25 He, X., Larson, J. M., Bechtel, H. A. & Kostecki, R. In situ infrared nanospectroscopy of the local processes at the Li/polymer electrolyte interface. *Nat. Commun.* **13**, 1398 (2022).

26 Zhang, J. *et al.* Multifunctional solvent molecule design enables high-voltage Li-ion batteries. *Nat. Commun.* **14**, 2211 (2023).

27 Zhan, C., Wu, T., Lu, J. & Amine, K. Dissolution, migration, and deposition of transition metal ions in Li-ion batteries exemplified by Mn-based cathodes–a critical review. *Energy*

Environ. Sci. **11**, 243-257 (2018).

28 Fan, X. & Wang, C. High-voltage liquid electrolytes for Li batteries: progress and perspectives. *Chem. Soc. Rev.* **50**, 10486-10566 (2021).

29 Liu, T. *et al.* Understanding Co roles towards developing Co-free Ni-rich cathodes for rechargeable batteries. *Nat. Energy* **6**, 277-286 (2021).

30 Yang, C. *et al.* Engineering A Boron‐Rich Interphase with Nonflammable Electrolyte toward Stable Li|| NCM811 Cells Under Elevated Temperature. *Adv. Mater.* **36**, 2307220 (2024).

31 Yang, Y.-P. *et al.* Thermal Stability Analysis of Lithium-Ion Battery Electrolytes Based on Lithium Bis(trifluoromethanesulfonyl)imide-Lithium Difluoro(oxalato)Borate Dual-Salt. *Polymers* **13**, 707 (2021).

32 Jiang, L., Liang, C., Li, H., Wang, Q. & Sun, J. Safer triethyl-phosphate-based electrolyte enables nonflammable and high-temperature endurance for a lithium ion battery. *ACS Appl. Energy Mater.* **3**, 1719-1729 (2020).

33 Yang, Y.-P. *et al.* Thermal stability analysis of lithium-ion battery electrolytes based on lithium bis (trifluoromethanesulfonyl) imide-lithium difluoro (oxalato) borate dual-salt. *Polymers* **13**, 707 (2021).

34 Jamil, S. *et al.* Ni/Li antisite induced disordered passivation layer for high-Ni layered oxide cathode material. *Energy Storage Mater.* **45**, 720-729 (2022).

35 Lin, T. *et al.* Faster activation and slower capacity/voltage fading: a bifunctional urea treatment on lithium‐rich cathode materials. *Adv. Funct. Mater.* **30**, 1909192 (2020).

Acknowledgements

This work was supported by National Natural Science Foundation of China (92372207 and 22075174), the Science and Technology Commission of Shanghai Municipality (20520740900 and 19DZ2271100), the China Postdoctoral Science Foundation (2024T170794 and 2024M762822), the Zhejiang Province Postdoctoral Scientific Research Project (ZJ2024049), and International Joint Laboratory on Resource Chemistry. We thank the Quzhou Institute of Power Battery and Grid Energy Storage for providing the pouch cells.

Author contributions

S.X. conceived the idea, performed the experiment, and wrote the manuscript. Q.G. and S.G. performed molecular dynamics simulations. L.Z. R.G. and X.G. contributed to result discussion and data analysis. J.X., S.Z., Q.X., P.S., X.Z., Y.M. and J.L. supervised this work, discussed the results, and revised this manuscript.

Conflict of interest

The authors declare no conflict of interest.

Editorial Summary

High-voltage lithium-metal batteries face safety and stability challenges. Here, authors develop a non-flammable triethyl phosphate-based electrolyte using a triple-salt solute strategy to induce a bilayer solid electrolyte interphase, enabling long-term cycling of 4.5 V Li metal batteries.

Peer review information: *Nature Communications* thanks Yulin Jie, and the other, anonymous, reviewer(s) for their contribution to the peer review of this work. A peer review file is available.